ACS MATERIALS LETTERS

www.acsmaterialsletters.org

LETTER

Confined Synthesis of Ultrathin Amorphous Metal-Oxide Nanosheets

Binbin Jia, Jie Yang, Rui Hao, Lidong Li,* and Lin Guo*

Cite This: ACS Materials Lett. 2020, 2, 610–615

Read Online

ACCESS | Metrics & More | Article Recommendations | Supporting Information

ABSTRACT: As a new member of metal oxide family, two-dimensional (2D) amorphous metal oxide nanosheets have attracted considerable research interest in various fields, because of their unique surface electronic structure. However, some 2D amorphous metal oxide nanosheets produced by strong acid weak alkali salts (such as $FeCl_3$, $ZrCl_4$, $CrCl_3$, $SnCl_4$, and $AlCl_3$) are difficult to synthesize, because of their tendency to precipitate and aggregate under facile conditions. Thus, developing a common route to prepare these 2D amorphous metal oxide nanosheets is urgently needed. Herein, we report a universal method to synthesize a series of 2D amorphous metal oxide, including Fe_2O_3, Cr_2O_3, ZrO_2, SnO_2, and Al_2O_3. In this method, lamellar oleate is introduced as a host matrice to restrict the ion exchange reaction that occurs between Cu_2O and metal ions. By controlling calcination temperature to remove the oleate, the corresponding 2D amorphous metal oxide ultrathin nanosheets are successfully obtained. This facial method may open a new avenue to fabricate promising 2D amorphous metal oxide nanosheets for practical applications.

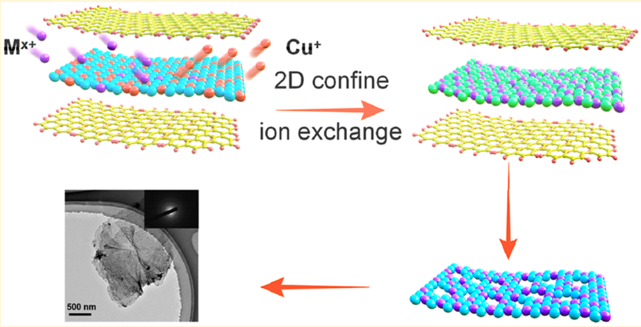

As a class of disordered structure with many dangling bonds, activity sites, and ion channels, amorphous metal oxides have attracted extensive attention in recent years, because of its superior performance in energy storage, catalysis, and mechanics.[1−5] Compared to two-dimensional (2D) crystalline metal-oxide nanomaterials, 2D films at amorphous state are isotropic, lack grain boundaries, and possess more dangling bonds and reactive sites, which would exhibit some special physical and chemical properties.[6−10] For example, Yang et al. found that 2D amorphous NiO nanosheet can act as an efficient photocatalyst for solar H_2 evolution without any co-catalysts.[11] Zhao et al. reported self-supported iron−cobalt−nickel amorphous oxide nanosheets, which showed superior electrocatalytic activity toward oxygen evolution reaction with an overpotential of only 170 mV.[12] Therefore, the precise morphology and composition control of 2D amorphous metal oxide nanomaterials is of great significance. To date, some methods have been proposed for the preparation of 2D amorphous metal-oxide nanomaterials, including thermal decomposition methods,[13] redox methods,[14] and template-assisted methods.[15] However, some serious issues are still inevitable. For instance, strong acid weak alkali salts such as $FeCl_3$, $ZrCl_4$, $CrCl_3$, $SnCl_4$, and $AlCl_3$ easily precipitate and aggregate to form the corresponding metal oxide (called SAWA-MO) nanoparticles. Thus, 2D metal oxide nanosheets are difficult to obtain under facile conditions, let alone amorphous 2D nanosheets. To date, only a few preparation methods have been investigated to synthesize some specific 2D amorphous nanomaterials.[16] Developing a common method to fabricate 2D amorphous ultrathin nanosheet of SAWA-MOs remains a great challenge.

So far, confined synthesis of 2D crystalline nanomaterials has been developed as an extension of template-assisted synthetic strategy.[17−19] It refers to confining the reactants to the interlayer spaces of layered materials to guide the growth of nanomaterials. The layered materials with limited interlayer spaces function as a host matrice for the embedded guest molecules to undergo chemical transformation under appropriate conditions. At present, graphite,[20,21] layered double hydroxides,[22,23] and MXenes[24] have been recognized as effective hosts for the confined synthesis of many 2D crystalline nanomaterials, including 2D metals,[25] 2D carbon materials,[26,27] 2D polymers,[28,29] and 2D metal-organic frameworks (MOFs).[30,31] However, some inevitable issues still exist for most of 2D confined templates. For example, the layered

Received: March 24, 2020
Accepted: April 28, 2020
Published: April 28, 2020

double hydroxide templates are readily dissolved during the synthesis process of SAWA-MO nanosheets. As a template, graphite always requires high temperature to be removed, leading to the crystallization of SAWA-MOs. Thus, developing suitable host matrices to fabricate pure 2D amorphous metal-oxide nanosheets is highly needed.

Herein, we first propose a universal confined method to synthesize a series of amorphous SAWA-MO ultrathin nanosheets (Fe_2O_3, Cr_2O_3, ZrO_2, SnO_2, and Al_2O_3). In this method, lamellar oleate is introduced as a host matrice to restrict the Cu_2O template. Through a simple ion exchange reaction, Cu ions are replaced by our target metal ions (M^{x+}) to form the corresponding amorphous $M(OH)_x$-oleate complex intermediate. By controlling the calcination temperature, the corresponding 2D amorphous SAWA-MO ultrathin nanosheets are successfully obtained. This synthetic method opens a new pathway for economical preparation of amorphous SAWA-MO ultrathin nanosheets, which might be a class of promising nanomaterials for future energy-related devices.

In this study, some strong acid weak alkali salts ($FeCl_3$, $ZrCl_4$, $CrCl_3$, $SnCl_4$ and $AlCl_3$) were selected as our reactants. Table S1 in the Supporting Information shows the K_{sp} values of the corresponding metal hydroxide precursors. The general synthesis route of amorphous SAWA-MO ultrathin nanosheets is illustrated in Figure 1. In brief, the lamellar Cu_2O-oleate

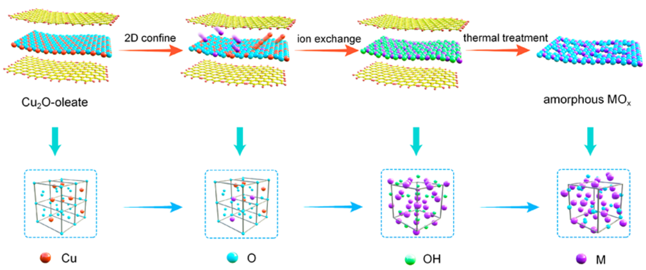

Figure 1. Schematic illustration for synthesis of amorphous SAWA-MO ultrathin nanosheets.

complex intermediate is employed as a 2D confined template. And then, Cu_2O undergoes a slow ion exchange reaction with M^{x+}. The generated metal hydroxide precursor is inserted into the interlamination of oleate to ensure the sheet structure. Through a simple low thermal treatment of $M(OH)_x$–oleate complex intermediate in an air atmosphere, the corresponding 2D amorphous SAWA-MO ultrathin nanosheets can be successfully obtained.

Taking 2D amorphous Fe_2O_3 ultrathin nanosheets as an example, lamellar Cu_2O-oleate complex intermediate is first synthesized by hydrothermal method and the size of nanosheets is at the micrometer level (Figure S1 in the Supporting Information).[32] Second, lamellar Cu_2O-oleate complex intermediate is dispersed in the solution ultrasonically. At the same time, a certain amount of NaCl aqueous solution is added to the suspension and vigorous stirring is needed to ensure NaCl aqueous solution is uniformly dispersed in the solution. And then, $FeCl_3$ solution is slowly added to the suspension with a constant pressure titration funnel. In this process, Fe^{3+} is introduced into the entire reaction system, which can react with Cu_2O to produce CuCl via ion exchange. Meanwhile, obtained CuCl can coordinate with extra Cl^- in the solution to form $CuCl_x^-$ and dissolve in the solution. With the occurrence of coordination reaction, it will further promote ion exchange between Fe^{3+} and Cu_2O. After the reaction is completed, an amorphous $Fe(OH)_3$-oleate complex intermediate can be successfully prepared (see Figure S2 in the Supporting Information). Because the entire reaction occurs in interlamination, the product can well maintain lamellar morphology of Cu_2O template. Finally, the obtained $Fe(OH)_3$-oleate complex intermediate is placed in a tube furnace for rapid low-temperature calcination to remove oleate intermediate and water molecules. In this process, choosing appropriate reaction temperature is significant.[32] If the temperature is too high, crystallization might occur (see Figure S3 in the Supporting Information). If the temperature is too low, oleate will not be completely removed (see Figure S4 in the Supporting Information). After the precipitate is collected, 2D amorphous Fe_2O_3 nanosheet can be successfully obtained.

The detailed morphological and structural characterizations of 2D amorphous Fe_2O_3 nanosheet are displayed in Figure 2.

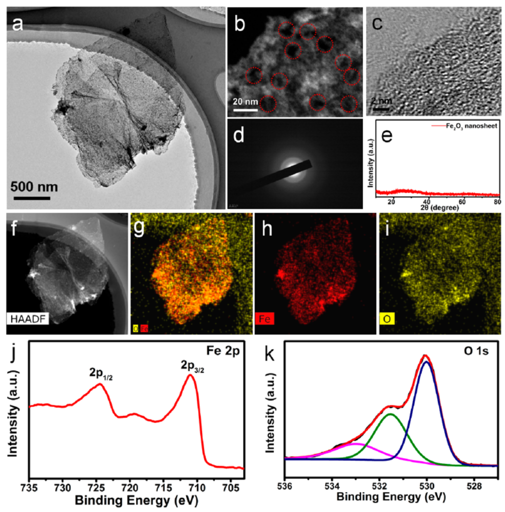

Figure 2. (a) TEM image of the 2D amorphous Fe_2O_3 nanosheet; (b) HAADF-STEM image of the 2D amorphous Fe_2O_3 nanosheet; (c) HRTEM image of the 2D amorphous Fe_2O_3 nanosheet; (d) the corresponding SAED pattern of the 2D amorphous Fe_2O_3 nanosheet; (e) XRD spectrum of the 2D amorphous Fe_2O_3 nanosheet; (f) HAADF-STEM image and (g–i) corresponding elemental mapping analysis (O and Fe (panel (g)), Fe only (panel (h)), and O only (panel (i))) of the 2D amorphous Fe_2O_3 nanosheet; and (j, k) XPS spectra of the 2D amorphous Fe_2O_3 nanosheet (Fe 2p (panel (j)) and O 1s (panel (k))).

The scanning electron microscopy (SEM) (see Figure S5 in the Supporting Information) and transmission electron microscopy (TEM) (Figure 2a) images reveal that a great amount of nanosheets have been successfully prepared, with uniform micrometer-size and ultrathin thickness, which is similar to the morphology of template. In addition, a partial stacking of nanosheets can be found in the TEM image. The main reason is that, during the process of removing oleate, water molecules will also be removed, leading to the reconstruction of ultrathin Fe_2O_3 nanosheets. As a result, nanosheets between the layers are partially stacked. Therefore, amorphous Fe_2O_3 nanosheets possess a monomolecular layer in the interlamination, but nanosheets are partially restructured during the calcination process, resulting in an increase in the thickness of nanosheets. Based on high-angle annular dark-field

https://dx.doi.org/10.1021/acsmaterialslett.0c00114
ACS Materials Lett. 2020, 2, 610–615

scanning transmission electron microscopy (HAADF-STEM) image, as shown in Figure 2b, it can be seen that nanosheets have a uniform pore structure with a size of 10 nm. HRTEM (Figure 2c) shows that no fringe lattices can be observed, indicating its amorphous nature. Detailed structural features are characterized by employing the corresponding selected-area electron-diffraction pattern (SAED) and X-ray diffraction pattern (XRD). The SAED pattern (Figure 2d) also displays its amorphous nature, which is consistent with the result of XRD spectrum (Figure 2e). The elemental mapping analyses of 2D amorphous Fe_2O_3 nanosheet, as shown in Figures 2f–i, reveal that Fe and O are homogeneously distributed across the entire nanosheet. Moreover, the chemical state and local atomic structure of our sample are studied by X-ray photoelectron spectroscopy (XPS). As shown in Figure 2j, Fe $2p_{3/2}$ and Fe $2p_{1/2}$ peaks are located at 711.0 and 724 eV, respectively, which belong to the Fe^{3+} characteristic peak. The peaks at 718 and 732.4 eV are the satellite peaks corresponding to Fe $2p_{3/2}$ and Fe $2p_{1/2}$, respectively.[33] Figure 2k shows the XPS spectra and curve fitting results of O 1s. The three characteristic peaks located at 529.6, 531.3, and 532.8 eV can be attributed to lattice oxygen, oxygen in OH^-, and bound water, respectively.[34] Based on all of the above analysis, it proves that ultrathin amorphous porous Fe_2O_3 nanosheets have been successfully prepared. In addition, to characterize the purity of amorphous Fe_2O_3 nanosheets, the XPS spectrum of Cu 2p in the Fe_2O_3 is displayed in Figure S6 in the Supporting Information. It can be seen that a small amount of Cu components also exist, but the relative intensity of Cu peak is very low. The mass ratio of Fe and Cu tested by XPS is ~98.64:1.36, indicating the high purity of our product.

Taking the amorphous Fe_2O_3 nanosheet as an example, the possible formation mechanism for 2D amorphous structure is suggested. First, 2D amorphous $Fe(OH)_3$ precursor is produced by a confined reaction. In order to prove the reaction occurs between layers of oleate, XRD spectra of Cu_2O-oleate intermediate, $Fe(OH)_3$-oleate intermediate, and Fe_2O_3 are shown in Figure 3a. It can be clearly seen that the Cu_2O-oleate complex intermediate has two sets of diffraction peaks. One is a very ordered periodic diffraction peak belonging to the peak of oleate (006, 007), indicating that the oleate has a layered structure. The other set is the diffraction peaks of cubic phase Cu_2O. All the diffraction peaks (110, 111, 200, 211, 220, 311) are strong, demonstrating good crystallinity of Cu_2O, which is consistent with previous reports in the literature.[32] Whereas, as shown in XRD spectrum of Fe $(OH)_3$-oleate complex intermediate, only periodic diffraction peaks for layered structure of oleate (006, 007) remained, and Cu_2O crystal peaks disappeared, indicating that $Fe(OH)_3$ completely replaced Cu_2O through ion exchange reaction between layers of oleate, and $Fe(OH)_3$ nanosheet is amorphous. Moreover, when we compared the scanning electron microscopy (SEM) image of Cu_2O-oleat complex with that of an $Fe(OH)_3$-oleate complex intermediate (see Figures S1 and S2 in the Supporting Information), it can be seen that the morphologies remained, and no nanoparticles were visible on the edge or surface, further confirming that the ion exchange reaction happened between the layers of oleate. The elemental mapping analyses of both the surface and cross section show that elemental Fe and O are uniformly distributed on the nanosheets, revealing the existence of $Fe(OH)_3$ in the precursor (Figures 3b and 3c). During the interlayer reaction, the original lattice structure of Cu_2O is destroyed, making the $Fe(OH)_3$ precursor an amorphous state. In the subsequent calcination reactions, amorphous Fe_2O_3 nanosheets can be readily obtained as long as an appropriate temperature is applied.

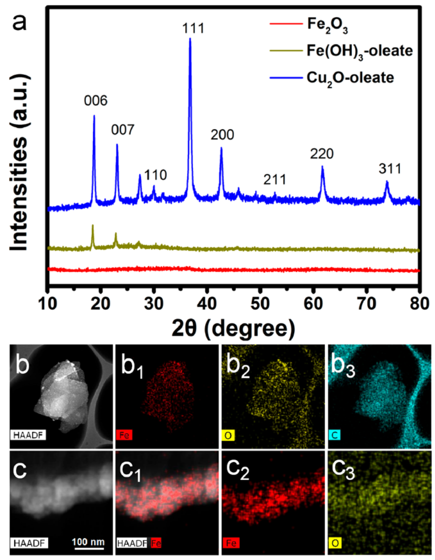

Figure 3. (a) XRD spectra of the Cu_2O-oleate complex intermediate, the $Fe(OH)_3$-oleate complex intermediate, and the Fe_2O_3 nanosheet; (b) corresponding elemental mapping analysis of the $Fe(OH)_3$-oleate complex intermediate; and (c) cross-sectional elemental mapping analysis of the $Fe(OH)_3$-oleate complex intermediate.

In order to test the universality of this confined method, different SAWA salts are added into the solution. Herein, by adjusting the ratio of ethanol and water, the amount of Cu_2O and metal salts, and appropriate heat treatment temperature, a series of amorphous SAWA-MO nanosheets have been successfully synthesized, including SnO_2, Cr_2O_3, ZrO_2 and Al_2O_3 nanosheets. SEM (Figure S7 in the Supporting Information) and TEM images (Figures 4a–d) indicate that SAWA-MO nanosheets basically retained the morphology of original Cu_2O template nanosheets. The HRTEM images in Figures $4a_1$–d_1 reveal that the as-synthesized SAWA-MO nanosheets are amorphous, as evidenced by the absence of typical lattice fringes, which is in agreement with the corresponding SAED images (see the insets in Figures 4a–d). In addition, no additional crystalline peaks can be seen in the XRD pattern (Figure S8 in the Supporting Information), further confirming the amorphous nature of SAWA-MO nanosheets.

To characterize the electronic structure of various samples, XPS spectra of obtained samples are conducted, and the results are displayed in detail in Figures S9–S12 in the Supporting Information. Figure S9a in the Supporting Information shows XPS spectra of Sn 3d, the two symmetrical peaks are located at 487.0 and 495.5 eV, respectively, corresponding to Sn $3d_{5/2}$ and Sn $3d_{3/2}$. In addition, the binding energy width (ΔE) of Sn $3d_{5/2}$ and Sn $3d_{3/2}$ is calculated to be 8.5 eV, which is close to the ΔE value of Sn^{4+} reported in the literature.[35] In addition, the O 1s spectrum is further conducted as shown in Figure S9b in the Supporting Information; the two O 1s peaks located at 530.4 and 531.8 eV can be ascribed to the lattice oxygen and OH^-, respectively. All of the above features suggest that our synthesized sample is SnO_2. For the Cr 2p XPS spectrum (Figure S10a in the Supporting Information), the peaks fitted

https://dx.doi.org/10.1021/acsmaterialslett.0c00114
ACS Materials Lett. 2020, 2, 610–615

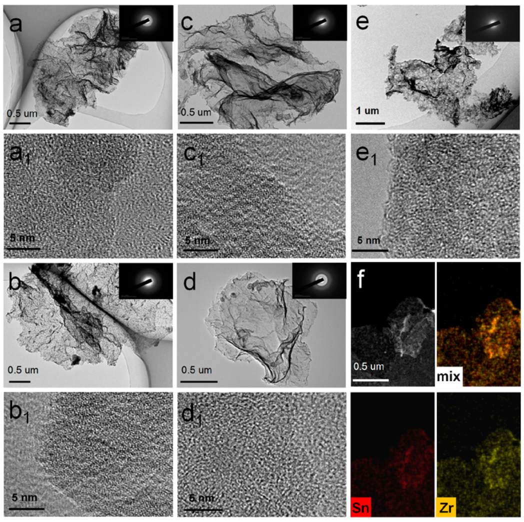

Figure 4. (a–e) TEM images of 2D amorphous SAWA-MO ultrathin nanosheets (SnO_2 (panel (a)), Cr_2O_3 (panel (b)), ZrO_2 (panel (c)), Al_2O_3 (panel (d)), and $SnZrO_x$ (panel (e))) (the inset images show the corresponding SAED patterns); (a_1–e_1) HRTEM images of 2D amorphous SAWA-MO ultrathin nanosheets (SnO_2(panel (a_1)), Cr_2O_3 (panel (b_1)), ZrO_2 (panel (c_1)), Al_2O_3 (panel (d_1)), and $SnZrO_x$ (panel (e_1)); and (f) elemental mapping analysis of the $SnZrO_x$ nanosheet.

at 576.6 and 586.5 eV correspond to Cr $2p_{3/2}$ and Cr $2p_{1/2}$, respectively, indicating the presence of Cr^{3+}. The peaks at 529.8, 531.4, and 532.8 eV in the O 1s spectrum (Figure S10b in the Supporting Information) should be assigned to lattice oxygen, OH^-, and bound water, respectively. All of the above observations strongly support the successful synthesis of Cr_2O_3.[36] As shown in Figure S11a in the Supporting Information, two distinct characteristic peaks of Zr 3d, located at 182.2 and 184.6 eV, correspond to Zr $3d_{5/2}$ and Zr $3d_{3/2}$, respectively, suggesting the existence of Zr^{4+}. The O 1s spectrum (Figure S11b in the Supporting Information) possesses two distinct characteristic peaks at 529.9 and 531.8 eV, corresponding to lattice oxygen and OH^-, respectively, which indicate the successful synthesis of ZrO_2.[16] Similarly, the XPS spectrum of Al_2O_3 2p (Figure S12a in the Supporting Information) show that only one main peak is located at 74.3 eV, which can be ascribed to Al^{3+}. The O 1s spectrum (Figure S12b) shows only a particularly symmetrical characteristic peak at 531.6 eV, which can be assigned to lattice oxygen. The above analysis results identify the presence of Al_2O_3.[13]

For the amorphous SAWA-MO nanosheet, it is difficult to precisely control element composition to obtain the corresponding binary amorphous metal oxides, because of the different reaction kinetics and redox potential of different metal ions.[6,37] However, because of synergistic effect between different elements, the properties of binary metal oxides are generally improved, compared to those of mono-metal oxides. In this synthesis method, unlike other methods for preparing binary amorphous metal oxides, metal salts react with Cu_2O, based on ion exchange; thus, the reaction rate is less affected by the solubility product constant. Therefore, this method is suitable for the synthesis of amorphous bimetallic metal oxide nanosheets. Taking the synthesis of amorphous $SnZrO_x$ nanosheets as an example, Figure 4e shows a TEM image of the $SnZrO_x$ nanosheets. It can be seen that the nanosheets have a similar morphology and size to that of Cu_2O nanosheets. The selected-area electron diffraction (SAED) suggests that the $SnZrO_x$ nanosheet possesses an amorphous structure, which is consistent with the HRTEM results (Figure 4e_1) and the XRD results (see Figure S13 in the Supporting Information). Mapping analysis (Figure 4f) reveals the homogeneous distribution of Sn and Zr in amorphous $SnZrO_x$ nanosheets. Based on the above analyses of the $SnZrO_x$ nanosheets, it is confirmed that our method can be extended to the synthesis of 2D multiple amorphous SAWA-MO nanosheets.

Metal oxides have always been considered to be a class of excellent anode materials, because of their high theoretical capacities.[38,39] In order to verify advantages of amorphous materials in energy storage, the cycling performance of pure amorphous Fe_2O_3 (a-Fe_2O_3) nanosheet as an anode material for potassium-ion batteries is first evaluated (see Figure S14 in the Supporting Information), as well as crystalline Fe_2O_3 (c-Fe_2O_3) nanosheet (see Figures S3 and S15 in the Supporting Information) for comparison. It is obvious to see that c-Fe_2O_3 nanosheet basically has no potassium electric properties and the reversible capacity directly decreased to 20 mAh g^{-1} at 0.1 A g^{-1} after 100 cycles. Compared to c-Fe_2O_3 electrode, the amorphous Fe_2O_3 electrode has better cycling performance. The initial capacity of a-Fe_2O_3 nanosheet potassium has reached 450 mAh g^{-1}, and the capacity still possesses 210 mAh g^{-1} at 0.1 A g^{-1} after 100 cycles, which can be attributed to the flexible amorphous porous structure buffered volume change during potassium ion intercalation and deintercalation process. Therefore, amorphous Fe_2O_3 nanosheets have promising application potential in potassium-ion batteries by combining with other conductive materials.

In summary, we successfully developed a simple and universal synthetic strategy to create a series of 2D amorphous SAWA-MO nanosheets. The key step of this approach is to confine the amorphous metal hydroxide precursor to the interlamination of oleate. This method can not only be used to synthesize amorphous mono-metal oxide nanosheets (Fe_2O_3, SnO_2, Cr_2O_3, ZrO_2, Al_2O_3), but can also be extended to the synthesis of amorphous binary metal oxide nanosheets ($SnZrO_x$). Compared to the 2D crystalline Fe_2O_3 nanosheet, 2D amorphous Fe_2O_3 nanosheet shows great application potential in potassium-ion batteries. Overall, this method broadens the variety of 2D amorphous metal oxide nanomaterials and provides important guidance for the synthesis of other 2D amorphous nanomaterials.

■ ASSOCIATED CONTENT

Supporting Information

The Supporting Information is available free of charge at https://pubs.acs.org/doi/10.1021/acsmaterialslett.0c00114.

> Details regarding the synthesis of the lamellar Cu_2O-oleate complex intermediate, the 2D amorphous Fe_2O_3 nanosheet, the 2D amorphous SnO_2 nanosheet, the 2D amorphous Cr_2O_3 nanosheet, the 2D amorphous ZrO_2 nanosheet, the 2D amorphous Al_2O_3 nanosheet, the 2D amorphous $SnZrO_x$ nanosheet, and the 2D crystalline Fe_2O_3 nanosheet; material characterizations; supplemental figures S1–S15; Table S1 (PDF)

AUTHOR INFORMATION

Corresponding Authors

Lin Guo − *School of Chemistry, Beijing Advanced Innovation Center for Biomedical Engineering, Beihang University, Beijing 100191, China*; orcid.org/0000-0002-6070-2384; Email: guolin@buaa.edu.cn

Lidong Li − *School of Chemistry, Beijing Advanced Innovation Center for Biomedical Engineering, Beihang University, Beijing 100191, China*; Email: lilidong@buaa.edu.cn

Authors

Binbin Jia − *School of Chemistry, Beijing Advanced Innovation Center for Biomedical Engineering, Beihang University, Beijing 100191, China*

Jie Yang − *School of Chemistry, Beijing Advanced Innovation Center for Biomedical Engineering, Beihang University, Beijing 100191, China*

Rui Hao − *School of Chemistry, Beijing Advanced Innovation Center for Biomedical Engineering, Beihang University, Beijing 100191, China*

Complete contact information is available at:
https://pubs.acs.org/10.1021/acsmaterialslett.0c00114

Author Contributions

L.G., L.L., and B.J. conceived the research project. B.J. designed, synthesized, and characterized the materials and investigated the electrochemical properties. J.Y. performed the TEM studies. R.H. gave some suggestions for the manuscript. All authors contributed to the data analysis and commented on the manuscript.

Notes

The authors declare no competing financial interest.

ACKNOWLEDGMENTS

We acknowledge the funding support by National Natural Science Foundation of China (Nos. 51532001, 51872016, and 51772011).

ABBREVIATIONS

2D, two-dimensional; SAWA-MO, strong acid weak alkali salts corresponding metal oxide; SEM, scanning electron microscopy; TEM, transmission electron microscopy; HAADF-STEM, high-angle annular dark-field scanning transmission electron microscopy; SAED, selected-area electron-diffraction pattern; XRD, X-ray diffraction pattern; XPS, X-ray photoelectron spectroscopy; a-Fe_2O_3, amorphous Fe_2O_3; c-Fe_2O_3, crystalline Fe_2O_3

REFERENCES

(1) Smith, R. D.; Prévot, M. S.; Fagan, R. D.; Zhang, Z.; Sedach, P. A.; Siu, M. K. J.; Trudel, S.; Berlinguette, C. P. Photochemical route for accessing amorphous metal oxide materials for water oxidation catalysis. *Science* **2013**, *340*, 60−63.

(2) Jiang, Y.; Zhang, D.; Li, Y.; Yuan, T.; Bahlawane, N.; Liang, C.; Sun, W.; Lu, Y.; Yan, M. Amorphous Fe_2O_3 as a high-capacity, high-rate and long-life anode material for lithium ion batteries. *Nano Energy* **2014**, *4*, 23−30.

(3) Yan, S.; Abhilash, K.; Tang, L.; Yang, M.; Ma, Y.; Xia, Q.; Guo, Q.; Xia, H. Research advances of amorphous metal oxides in electrochemical energy storage and conversion. *Small* **2018**, *15*, 1804371.

(4) Kuai, L.; Geng, J.; Chen, C.; Kan, E.; Liu, Y.; Wang, Q.; Geng, B. A reliable aerosol-spray-assisted approach to produce and optimize amorphous metal oxide catalysts for electrochemical water splitting. *Angew. Chem., Int. Ed.* **2014**, *53*, 7547−7551.

(5) Choi, I. Y.; Jo, C.; Lim, W.-G.; Han, J.-C.; Chae, B.-G.; Park, C. G.; Lee, J.; Kim, J. K. Amorphous Tin Oxide Nanohelix Structure Based Electrode for Highly Reversible Na-Ion Batteries. *ACS Nano* **2019**, *13*, 6513−6521.

(6) Jia, B.; Hao, R.; Huang, Z.; Hu, P.; Li, L.; Zhang, Y.; Guo, L. Creating ultrathin amorphous metal hydroxide and oxide nanosheet libraries. *J. Mater. Chem. A* **2019**, *7*, 4383−4388.

(7) Jia, B.; Chen, W.; Luo, J.; Yang, Z.; Li, L.; Guo, L. Construction of MnO_2 Artificial Leaf with Atomic Thickness as Highly Stable Battery Anodes. *Adv. Mater.* **2020**, *32*, 1906582.

(8) Liu, W.; Xu, Q.; Cui, W.; Zhu, C.; Qi, Y. CO_2-Assisted Fabrication of Two-Dimensional Amorphous Molybdenum Oxide Nanosheets for Enhanced Plasmon Resonances. *Angew. Chem., Int. Ed.* **2017**, *56*, 1600−1604.

(9) Wang, X.; Shi, W.; Wang, S.; Zhao, H.; Lin, J.; Yang, Z.; Chen, M.; Guo, L. Two-dimensional amorphous TiO_2 nanosheets enabling high-efficiency photoinduced charge transfer for excellent SERS activity. *J. Am. Chem. Soc.* **2019**, *141*, 5856−5862.

(10) Li, Y.; Hao, J.; Song, H.; Zhang, F.; Bai, X.; Meng, X.; Zhang, H.; Wang, S.; Hu, Y.; Ye, J. Selective light absorber-assisted single nickel atom catalysts for ambient sunlight-driven CO_2 methanation. *Nat. Commun.* **2019**, *10*, 2359.

(11) Lin, Z.; Du, C.; Yan, B.; Wang, C.; Yang, G. Two-dimensional amorphous NiO as a plasmonic photocatalyst for solar H_2 evolution. *Nat. Commun.* **2018**, *9*, 4036.

(12) Fan, J.; Chen, Z.; Shi, H.; Zhao, G. In situ grown, self-supported iron-cobalt-nickel alloy amorphous oxide nanosheets with low overpotential toward water oxidation. *Chem. Commun.* **2016**, *52*, 4290−4293.

(13) Zhao, C.; Zhang, H.; Si, W.; Wu, H. Mass production of two-dimensional oxides by rapid heating of hydrous chlorides. *Nat. Commun.* **2016**, *7*, 12453.

(14) Xu, C.; Shi, S.; Sun, Y.; Chen, Y.; Kang, F. Ultrathin amorphous manganese dioxide nanosheets synthesized with controllable width. *Chem. Commun.* **2013**, *49*, 7331−7333.

(15) Zhao, H.; Yue, Y.; Zhang, Y.; Li, L.; Guo, L. Ternary artificial nacre reinforced by ultrathin amorphous alumina with exceptional mechanical properties. *Adv. Mater.* **2016**, *28*, 2037−2042.

(16) Zhao, H.; Zhu, Y.; Li, F.; Hao, R.; Wang, S.; Guo, L. A Generalized Strategy for the Synthesis of Large-Size Ultrathin Two-Dimensional Metal Oxide Nanosheets. *Angew. Chem., Int. Ed.* **2017**, *56*, 8766−8770.

(17) Li, Z.; Zhang, X.; Cheng, H.; Liu, J.; Shao, M.; Wei, M.; Evans, D. G.; Zhang, H.; Duan, X. Confined Synthesis of 2D Nanostructured Materials toward Electrocatalysis. *Adv. Energy Mater.* **2020**, *10*, 1900486.

(18) Dong, R.; Zhang, T.; Feng, X. Interface-assisted synthesis of 2D materials: Trend and challenges. *Chem. Rev.* **2018**, *118*, 6189−6235.

(19) Zheng, X.; Xu, J.; Yan, K.; Wang, H.; Wang, Z.; Yang, S. Space-confined growth of MoS_2 nanosheets within graphite: the layered hybrid of MoS_2 and graphene as an active catalyst for hydrogen evolution reaction. *Chem. Mater.* **2014**, *26*, 2344−2353.

(20) Allen, M. J.; Tung, V. C.; Kaner, R. B. Honeycomb carbon: a review of graphene. *Chem. Rev.* **2010**, *110*, 132−145.

(21) Zhang, Y.; Zhang, L.; Zhou, C. Review of chemical vapor deposition of graphene and related applications. *Acc. Chem. Res.* **2013**, *46*, 2329−2339.

(22) Li, Z.; Duan, H.; Shao, M.; Li, J.; O'Hare, D.; Wei, M.; Wang, Z. L. Ordered-vacancy-induced cation intercalation into layered double hydroxides: A general approach for high-performance supercapacitors. *Chem.* **2018**, *4*, 2168−2179.

(23) Shao, M.; Zhang, R.; Li, Z.; Wei, M.; Evans, D. G.; Duan, X. Layered double hydroxides toward electrochemical energy storage and conversion: design, synthesis and applications. *Chem. Commun.* **2015**, *51*, 15880−15893.

https://dx.doi.org/10.1021/acsmaterialslett.0c00114
ACS Materials Lett. 2020, 2, 610−615

(24) Naguib, M.; Mochalin, V. N.; Barsoum, M. W.; Gogotsi, Y. 25th anniversary article: MXenes: a new family of two-dimensional materials. *Adv. Mater.* **2014**, *26*, 992−1005.

(25) Wang, L.; Zhu, Y.; Wang, J.-Q.; Liu, F.; Huang, J.; Meng, X.; Basset, J.-M.; Han, Y.; Xiao, F.-S. Two-dimensional gold nanostructures with high activity for selective oxidation of carbon-hydrogen bonds. *Nat. Commun.* **2015**, *6*, 6957.

(26) Liu, W.; Xu, S.; Guan, S.; Liang, R.; Wei, M.; Evans, D. G.; Duan, X. Confined synthesis of carbon nitride in a layered host matrix with unprecedented solid-state quantum yield and stability. *Adv. Mater.* **2018**, *30*, 1704376.

(27) Song, L.; Shi, J.; Lu, J.; Lu, C. Structure observation of graphene quantum dots by single-layered formation in layered confinement space. *Chem. Sci.* **2015**, *6*, 4846−4850.

(28) Boota, M.; Anasori, B.; Voigt, C.; Zhao, M. Q.; Barsoum, M. W.; Gogotsi, Y. Pseudocapacitive electrodes produced by oxidant-free polymerization of pyrrole between the layers of 2D titanium carbide (MXene). *Adv. Mater.* **2016**, *28*, 1517−1522.

(29) Wang, X.; Ma, Y.; Sheng, X.; Wang, Y.; Xu, H. Ultrathin polypyrrole nanosheets via space-confined synthesis for efficient photothermal therapy in the second near-infrared window. *Nano Lett.* **2018**, *18*, 2217−2225.

(30) Jahan, M.; Bao, Q.; Loh, K. P. Electrocatalytically active grapheme-porphyrin MOF composite for oxygen reduction reaction. *J. Am. Chem. Soc.* **2012**, *134*, 6707−6713.

(31) Zhao, L.; Dong, B.; Li, S.; Zhou, L.; Lai, L.; Wang, Z.; Zhao, S.; Han, M.; Gao, K.; Lu, M.; et al. Interdiffusion Reaction-Assisted Hybridization of Two-Dimensional Metal-Organic Frameworks and $Ti_3C_2T_x$ Nanosheets for Electrocatalytic Oxygen Evolution. *ACS Nano* **2017**, *11*, 5800−5807.

(32) Gao, S.; Sun, Y.; Lei, F.; Liu, J.; Liang, L.; Li, T.; Pan, B.; Zhou, J.; Xie, Y. Freestanding atomically-thin cuprous oxide sheets for improved visible-light photoelectrochemical water splitting. *Nano Energy* **2014**, *8*, 205−213.

(33) Hu, Y.; Guan, C.; Ke, Q.; Yow, Z. F.; Cheng, C.; Wang, J. Hybrid Fe_2O_3 nanoparticle clusters/rGO paper as an effective negative electrode for flexible supercapacitors. *Chem. Mater.* **2016**, *28*, 7296−7303.

(34) Li, D.; Zhou, J.; Chen, X.; Song, H. Amorphous Fe_2O_3/graphene composite nanosheets with enhanced electrochemical performance for sodium-ion battery. *ACS Appl. Mater. Interfaces* **2016**, *8*, 30899−30907.

(35) Song, H.; Zhang, L.; He, C.; Qu, Y.; Tian, Y.; Lv, Y. Graphene sheets decorated with SnO_2 nanoparticles: in situ synthesis and highly efficient materials for cataluminescence gas sensors. *J. Mater. Chem.* **2011**, *21*, 5972−5977.

(36) Zhang, Y.; Qiu, W.; Ma, Y.; Luo, Y.; Tian, Z.; Cui, G.; Xie, F.; Chen, L.; Li, T.; Sun, X. High-performance electrohydrogenation of N_2 to NH_3 catalyzed by multishelled hollow Cr_2O_3 microspheres under ambient conditions. *ACS Catal.* **2018**, *8*, 8540−8544.

(37) Yang, Y.; Dang, L.; Shearer, M. J.; Sheng, H.; Li, W.; Chen, J.; Xiao, P.; Zhang, Y.; Hamers, R. J.; Jin, S. Highly active trimetallic NiFeCr layered double hydroxide electrocatalysts for oxygen evolution reaction. *Adv. Energy Mater.* **2018**, *8*, 1703189.

(38) Hu, Y.-Y.; Liu, Z.; Nam, K.-W.; Borkiewicz, O. J.; Cheng, J.; Hua, X.; Dunstan, M. T.; Yu, X.; Wiaderek, K. M.; Du, L.-S.; et al. Origin of additional capacities in metal oxide lithium-ion battery electrodes. *Nat. Mater.* **2013**, *12*, 1130−1136.

(39) Xu, S.; Hessel, C. M.; Ren, H.; Yu, R.; Jin, Q.; Yang, M.; Zhao, H.; Wang, D. α-Fe_2O_3 multi-shelled hollow microspheres for lithium ion battery anodes with superior capacity and charge retention. *Energy Environ. Sci.* **2014**, *7*, 632−637.

https://dx.doi.org/10.1021/acsmaterialslett.0c00114
ACS Materials Lett. 2020, 2, 610−615